Chapter 10

Unsteady Mixed Convection from Two Isothermal Semicircular Cylinders in Tandem Arrangement

Erick Salcedo, César Treviño, Juan C. Cajas and Lorenzo Martínez-Suástegui

Additional information is available at the end of the chapter

http://dx.doi.org/10.5772/66692

Abstract

In this chapter, two-dimensional mixed convection heat transfer in a laminar cross-flow from two heated isothermal semicircular cylinders in tandem arrangement with their curved surfaces facing the oncoming flow and confined in a channel is studied numerically. The governing equations are solved using the control-volume method on a nonuniform orthogonal Cartesian grid. Using the immersed-boundary method for fixed Reynolds number of $Re_D = u_D D/\upsilon = 200$, Prandtl number of $Pr = 7$, blockage ratio of $BR = D/H = 0.2$ and nondimensional pitch ratio of $\sigma = L/D = 3$, the influence of buoyancy and the confinement effect are studied for Richardson numbers in the range $-1 \le Ri \le 1$. Here, u_D is the average longitudinal velocity based on the diameter of the semicylinder. The variation of the mean and instantaneous nondimensional velocity, vorticity and temperature distributions with Richardson number is presented along with the nondimensional oscillation frequencies (Strouhal numbers) and phase-space portraits of flow oscillation from each semicylinder. In addition, local and averaged Nusselt numbers over the surface of the semicylinders are also obtained. The results presented herein demonstrate how the buoyancy and wall confinement affect the wake structure, vortex dynamics and heat transfer characteristics.

Keywords: bluff bodies, tandem arrangement, blockage ratio, interference effects, wall effects

1. Introduction

The flow and heat transfer past bluff bodies of various cross-sectional geometries is important because of advances in heat exchanger technology, cooling of electronic components and chips of different shapes and sizes. Although the majority of these studies have focused on studying the cross-flow past bluff bodies such as cylinders of circular [1–6], elliptic [7–10], rectangular [11–15] and square cross-sections [16–20], there are fewer studies on the semicircular cylinder geometry [21–24]. Gode *et al*. [25] studied numerically the momentum and heat transfer characteristics of a two-dimensional (2D), incompressible and steady flow over a semicircular cylinder and pointed out that the wake ceases to be steady somewhere in the range of $120 \leq Re \leq 130$. Boisaubert and Texier [26] performed solid tracer visualizations to assess the effect of a splitter plate on the near-wake development of a semicircular cylinder for Reynolds numbers of $Re = 200$ and 400 and three splitter plate configurations. Their results show that for $Re = 400$, the splitter plate causes an increase in near-wake length, a decrease in near-wake maximum width, a secondary vortex formation and a decrease of the maximum velocity in the recirculating zone, while for $Re = 200$, the near-wake keeps its symmetry and vortex shedding is inhibited. Nalluri *et al*. [27] solved numerically the coupled momentum and energy equations for buoyancy-assisted mixed convection from an isothermal hemisphere in Bingham plastic fluids and reported results for streamline and isotherm contours, local and mean Nusselt number as a function of the Reynolds, Prandtl, Richardson and Bingham numbers. Bhinder *et al*. [28] studied numerically the wake dynamics and forced convective heat transfer past an unconfined semicircular cylinder at incidence using air as the working fluid for Reynolds numbers in the range of $80 \leq Re \leq 180$ and angles of incidence in the range of $0^o \leq \alpha \leq 180^o$. Based on the flow pattern and the angle of incidence, they identified three flow distinct zones and proposed a correlation for the Strouhal and averaged Nusselt number as a function of Re and α. Chandra and Chhabra [29] performed a numerical study to assess the flow and thermal characteristics from a heated semicircular cylinder immersed in power-law fluids under laminar free and mixed convection for the case of buoyancy-assisted flow. Their results show that as the value of the Richardson and Reynolds numbers increase, the drag coefficient shows a monotonic increase and that the average Nusselt number increases with an increase in the value of the Reynolds, Prandtl and Richardson numbers.

The foregoing survey of literature reveals that although the great majority of research for the flow and heat transfer past a heated hemisphere in cross-flow has been made for an unbounded domain, there are relatively few studies that deal with the investigation of the blockage constraints present in the confined hemisphere problem. Kumar *et al*. [30] performed a numerical analysis to investigate the forced convection of power-law fluids (power-law index varying from 0.2 to 1.8) around a confined heated semicircular cylinder for Reynolds numbers between 1 and 40 and Prandtl number of 50. They assessed the effects of blockage ratios ranging from 0.16 to 0.50 and found that for a fixed value of Re, the length of the recirculation zone decreased with an increase in the value of n and that the drag coefficients and the averaged Nusselt number increased with increasing blockage ratio for any value of n.

From the foregoing discussion, it is clear that no prior results are available on the flow and heat transfer characteristics past a confined tandem hemisphere array under buoyancy-assisted and buoyancy-opposing conditions. This study aims to fill this void in the existing literature. In this work, we numerically investigate the transient fluid flow and thermal characteristics in the mixed convection regime around two isothermal semicylinders of the same diameter in tandem arrangement confined inside a vertical channel of finite length using fixed Reynolds and Prandtl numbers, fixed blockage ratio and gap width and several values of the buoyancy parameter (Richardson number).

2. Formulation of the problem

2.1. Governing equations and boundary conditions

Consider a 2D steady, Newtonian, incompressible Poiseuille flow fluid with a mean mainstream velocity u_0 at the entrance of a vertical duct over infinitely long semicylinders of diameter D placed symmetrically between two parallel plane walls as shown schematically in **Figure 1**. A system of Cartesian coordinates (x, y) is used with its origin located at the centre point of the upstream hemisphere. The length and height of the computational domain are defined in terms of the axial and lateral dimensions ($L_{\text{tot}} = 30D$ and H, respectively). The pitch-to-diameter ratio is $\sigma = L/D = 3$ and the blockage ratio $BR = D/H = 0.2$, where L is the longitudinal spacing between semicylinders. The upstream hemisphere is placed at a distance of 5.5D from the inlet to its centre and at a distance $S_1 = 24.5D$ from its centre to the outflow boundary. These values were chosen as they were estimated to be sufficiently large to allow the wake behind the downstream semicylinder to develop properly and to exit the domain without producing observable reflections. The forced flow enters the channel at ambient temperature T_0, and the semicylinders have a wall temperature of T_w. Flow rectifiers are placed at the channel exit producing a parallel flow at $x = S_1$. The thermophysical properties of the fluid are assumed to be constant except for the variation of density in the buoyancy term of the axial momentum equation (Boussinesq approximation) and the effect of viscous dissipation is neglected. Using the vorticity ($\Omega = \partial V/\partial X - \partial U/\partial Y$) and stream function formulation ($U = \partial\psi/\partial Y$, $V = -\partial\psi/\partial X$), the flow is described by the nondimensional equations

$$\frac{\partial^2\psi}{\partial X^2} + \frac{\partial^2\psi}{\partial Y^2} = -\Omega, \tag{1}$$

$$\frac{\partial\Omega}{\partial\tau} + \frac{\partial\psi}{\partial Y}\frac{\partial\Omega}{\partial X} - \frac{\partial\psi}{\partial X}\frac{\partial\Omega}{\partial Y} = \frac{1}{Re}\left(\frac{\partial^2\Omega}{\partial X^2} + \frac{\partial^2\Omega}{\partial Y^2}\right) + Ri\frac{\partial\theta}{\partial Y}, \tag{2}$$

$$\frac{\partial\theta}{\partial\tau} + \frac{\partial\psi}{\partial Y}\frac{\partial\theta}{\partial X} - \frac{\partial\psi}{\partial X}\frac{\partial\theta}{\partial Y} = \frac{1}{RePr}\left(\frac{\partial^2\theta}{\partial X^2} + \frac{\partial^2\theta}{\partial Y^2}\right). \tag{3}$$

where $\overline{V} = (U, V)$ is the dimensionless velocity vector and θ is the dimensionless temperature. In Eqs. (1)–(3), U and V are the X and Y components of $\overline{V}$, respectively. All velocity components are scaled with the oncoming mean bulk velocity u_0; the longitudinal and transverse coordinates are scaled with the semicylinder diameter D; the time is scaled with the residence time D/u_0, $\tau = tu_0/D$; the temperature is normalized as $\theta = (T-T_0)/(T_w-T_0)$. In the above equations, the nondimensional parameters are the Reynolds number, $Re = u_0D/\nu$, the Prandtl number $\Pr = \nu/\alpha$ and the Richardson number,

$Ri = g\beta(T_w - T_0)D/u_0^2$, respectively (frequently, instead of using the Richardson number, the Grashof number is employed, $Gr = RiRe^2 = g\beta(T_w - T_0)D^3/\nu^2$). Here, g is the acceleration due to gravity, α is the thermal diffusivity, β is the thermal expansion coefficient of the fluid and ν is the kinematic viscosity.

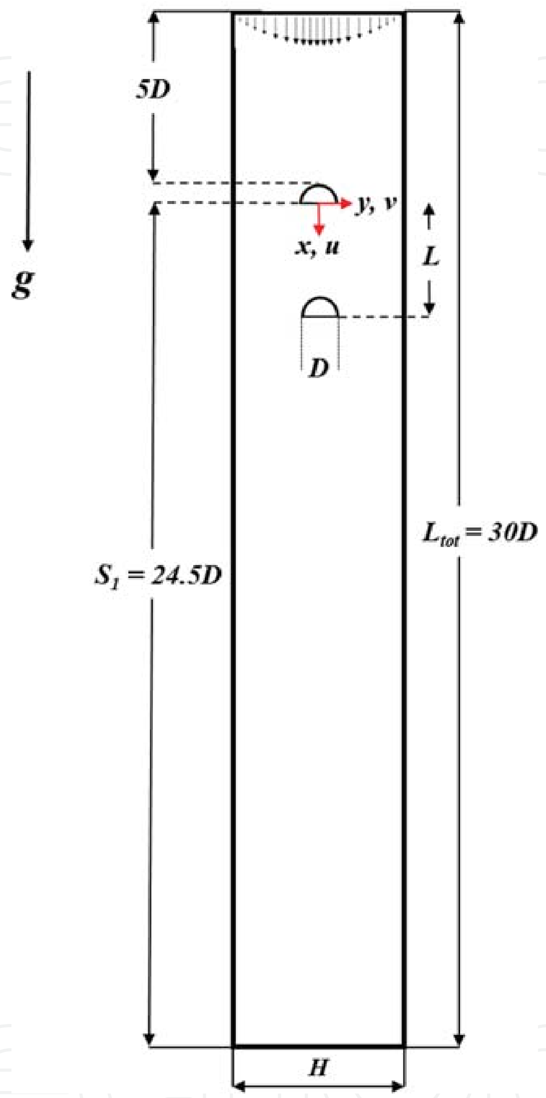

Figure 1. Schematic diagram of the computational domain and the configuration of the semicylinders inside the channel at $BR = 0.2$ and $\sigma = 3$.

Eqs. (1)–(3) have to be solved with the following boundary conditions:

The inflow boundary is specified by a developed velocity profile at the channel inlet

$$\psi - 1/2[1/BR + 3Y - 4(BR)^2 Y^3] = \Omega - 12(BR)^2 Y = \theta = 0, \quad (4)$$

For the channel walls, $\psi = 0, \ +1/BR$ at the left $\left(Y = -1/(2BR)\right)$ and right walls $\left(Y = +1/(2BR)\right)$, respectively. Vorticity at the walls is evaluated using Thom's first-order formula [31],

$$\Omega_w = 2(\psi_{w+1} - \psi_w)/\Delta n^2, \tag{5}$$

where Δn is the grid space normal to the wall. Adiabatic channel walls are assumed, $\partial\theta/\partial Y = 0$.

Homogeneous Neumann-type boundary conditions are adopted at the channel exit, provided that the outlet boundary is located sufficiently far downstream from the region of interest.

$$\partial\psi/\partial X|_{x=s_1} = \partial^2\psi/\partial X\partial Y|_{x=s_1} = \partial\theta/\partial X|_{x=s_1} = 0, \tag{6}$$

At the surface of the semicylinders,

$$\Omega - 2(\psi_{w+1} - \psi_w)/\Delta n^2 = \theta - 1 = 0. \tag{7}$$

No-normal and no-slip boundary conditions are enforced at the surface of each semicylinder. Due to the fact that the value of the stream function is an unknown constant along the surface of each hemisphere, its value is determined at each time step as part of the solution process [32].

With the temperature field known, the rate of heat flux q_j is obtained in nondimensional form with the local Nusselt number Nu_j, with $j = 1, 2$ for the upstream and downstream semicylinder, respectively. The local Nusselt numbers are evaluated from the following equation

$$Nu_j(S,\tau) = \frac{|q_j(S,t)|D}{(T_w - T_0)k} = \left|\frac{\partial\theta}{\partial n}\right|_S \tag{8}$$

where k is the thermal conductivity of the fluid and S is the surface of the immersed semicylinders. The surface-averaged (mean) Nusselt number is obtained by integrating the local Nusselt number along the surface of each semicylinder

$$\overline{Nu}_j(\tau) = \frac{1}{S}\int_S Nu_j(S,\tau)dS \tag{9}$$

2.2. Numerical solution

The governing equations are discretized using the power-law scheme described by Patankar [33] using a nonuniform staggered Cartesian grid with local grid refinements near the immersed semicylinders and near the channel walls. Eqs. (1)–(3) along with their corresponding boundary conditions are solved using a finite volume-based numerical method developed in Fortran 90 using parallel programming (OpenMP). Internal flow boundaries in the flow field are specified using the immersed boundary method [34]. For all computations, water is used as the cooling agent ($Pr = 7$). A stringent convergence criteria of the dependent variables of 1×10^{-7} is used, with an optimal time step of $\Delta\tau = 5\times10^{-4}$. A fully developed base flow is assigned as the initial value to each grid point in the domain, which physically means that both semicylinders are introduced into an isothermal fully developed cross-flow. For a given value of the Richardson number, computation is started immediately after the sudden imposition of a uniform wall nondimensional temperature from 0 to 1 on both semicylinders at time $\tau = 0$. Transient calculations are performed up to 500 nondimensional time units. In order to make comparisons with experimental results obtained on what are effectively unbounded domains, Chen *et al*. [35] defined a Reynolds number, $Re_D = u_D D/\nu$, where

$$u_D = \frac{1}{D} \int_{-D/2}^{D/2} u(y) dy. \tag{10}$$

In Eq. (10), u is the vertical component of the velocity field specified on the upstream boundary and u_D is the average longitudinal velocity based on the diameter of the semicylinder. The accuracy of the numerical algorithm was tested by comparing results of the mean Nusselt number against available analytical [2] and numerical results [35] for the standard case of a symmetrically confined isothermal circular cylinder in a plane channel. Details about the numerical solution, validation of the algorithm and the grid employed can be found elsewhere [36, 37].

3. Results and discussion

The numerical results presented in this work correspond in all cases to $Re_D = 200$, $Pr = 7$, $BR = 0.2$, and $\sigma = L/D = 3$. In this section, results are presented for the mean and instantaneous flow and thermal characteristics under varying thermal buoyancy. For clarity, only a portion of the computational domain is shown. The images display (from left to right) the nondimensional longitudinal and transverse velocity components with superimposed streamlines, the nondimensional vorticity field and the temperature field with superimposed velocity profiles. The color scales below each image map the velocity, vorticity and temperature contours, with red/yellow coloration representing positive vorticity or counterclockwise fluid rotation and the green regions reflecting a lack of rotational motion.

3.1. Response characteristics for assisting flow ($Ri = -1$)

In this section, the response characteristics for assisting flow are presented. **Figure 2** shows the resulting nondimensional mean flow and thermal profiles at $Ri = -1$ ($Gr = -4\times10^4$), illustrating how the relatively narrow wake of the upstream semicylinder reattaches at the forebody of the downstream semicylinder. Here, the near wake of the latter is clearly shorter and narrower and an increase in the longitudinal velocity component is observed at the central part of the channel ($Y = 0$) toward the downstream direction. The third strip illustrates how for the cooling process, the flow pattern is slightly asymmetric and the peak vorticity values are particularly large.

Figure 3 shows typical instantaneous flow and thermal patterns for $Ri = -1$, illustrating how small amplitude flow oscillation takes place within the gap, while Kármán vortices of relatively small size are shed from the rear face of the downstream semicylinder. The third strip shows how the interaction between the shear layers generated at the surface of both semicylinders and the channel walls increases toward the downstream direction and reaches a peak at a location of $X \approx 7$.

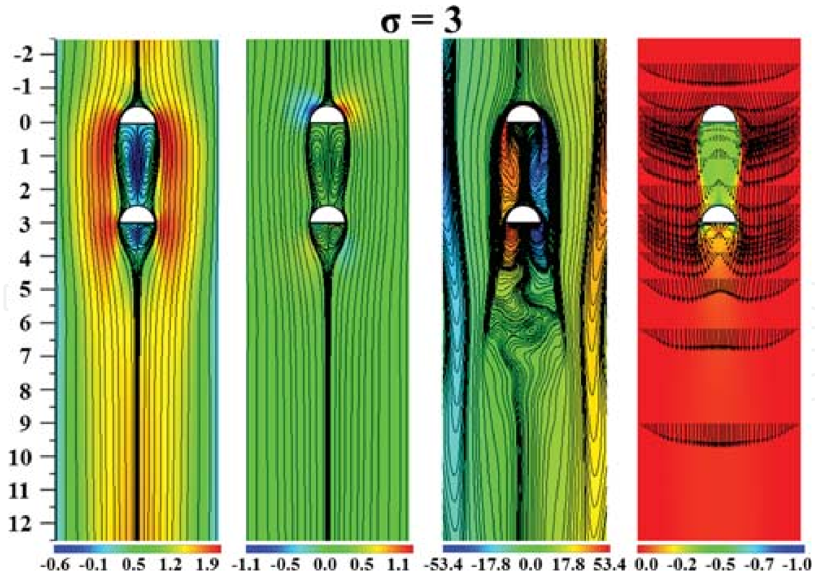

Figure 2. Nondimensional mean flow values at $Re_D = 200$, $BR = 0.2$, $\sigma = 3$ and $Ri = -1$ ($Gr = -4 \times 10^4$). From left to right: U and V velocity, Ω vorticity and θ temperature fields, respectively.

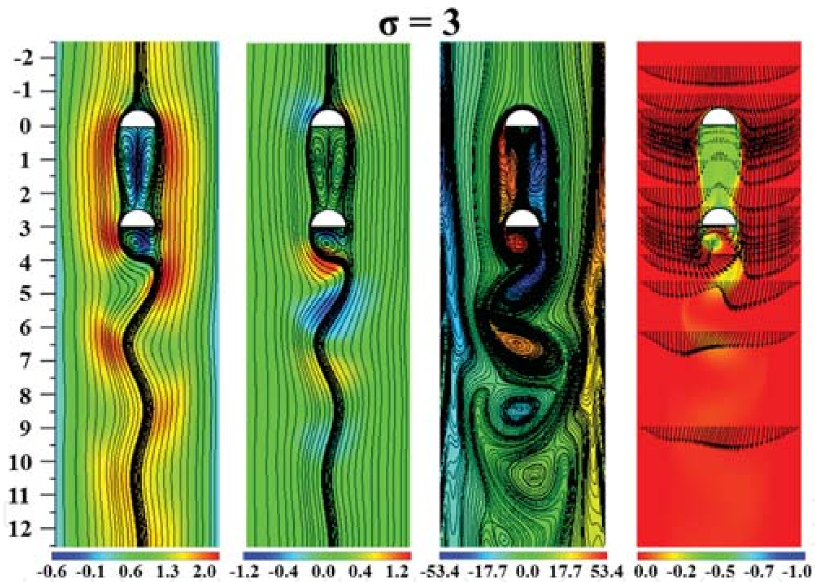

Figure 3. Nondimensional near wake patterns of instantaneous velocity, vorticity and temperature contours at $Re_D = 200$, $BR = 0.2$, $\sigma = 3$, and $Ri = -1$ ($Gr = -4 \times 10^4$). From left to right: U and V velocity, Ω vorticity and θ temperature fields, respectively.

Figure 4 shows the time variations of the nondimensional longitudinal and transverse velocity components at the symmetry plane and selected positions inside the channel. Clearly, the velocity fluctuations depict a harmonic behavior after a short induction time of $\tau \sim 100$. The inset of the top and bottom left images illustrates how the recirculation zone within the gap depicts small amplitude oscillations at a location of $(X, Y) = (1.5, 0)$, while the maximum amplitude of the velocity fluctuations is reached at a downstream position of $(X, Y) = (4.5, 0)$.

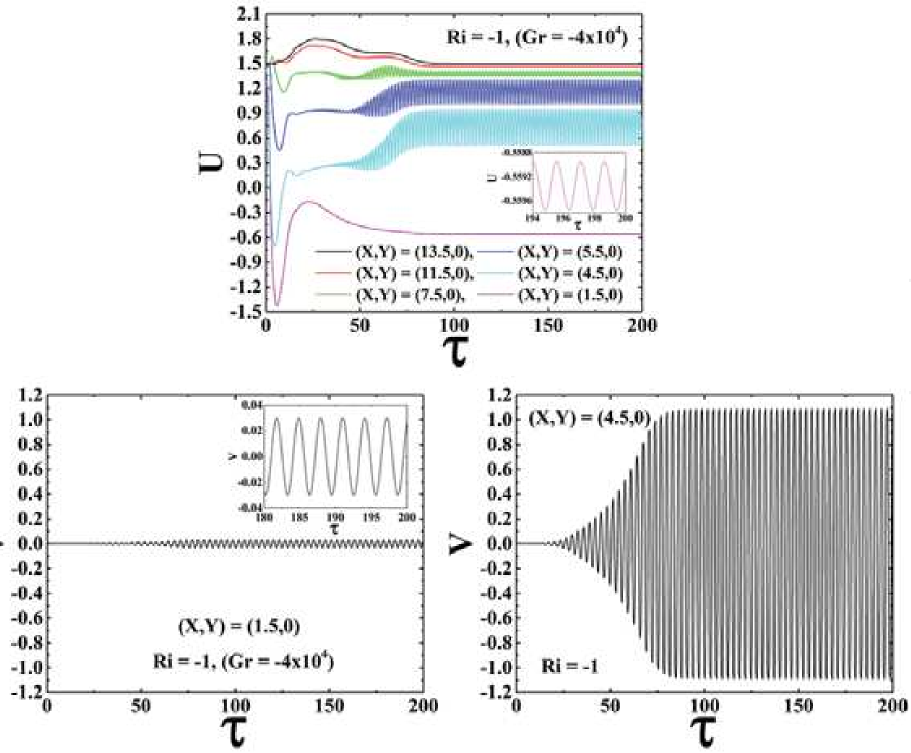

Figure 4. Time variations of the nondimensional longitudinal and transverse velocity components as a function of the nondimensional time at $Ri = -1$ ($Gr = -4{\times}10^4$). The extracted data is obtained at the symmetry plane and several X positions.

3.2. Response characteristics for isothermal flow ($Ri = 0$)

Figure 5 shows the nondimensional mean flow values for an isothermal flow ($Ri = 0$). In the absence of buoyancy, the mean flow solution is symmetric. Although the recirculation zone of the upstream semicylinder still occupies the total space within the gap, its width is now larger than the semicylinder diameter. In addition, the length of the near wake of the downstream semicylinder extends to $X{\approx}4.5$ and a slight decrease in vorticity strength takes place.

Figure 6 shows typical instantaneous patterns of velocity and vorticity illustrating how vortex shedding takes place at the rear of the downstream semicylinder. The third strip illustrates how in the absence of buoyancy, the interaction between the shear layers generated by the upstream semicylinder and the confining walls reduces.

Figure 7 shows the time variations of the nondimensional longitudinal and transverse velocity components at the symmetry plane and selected positions inside the channel. This image shows how after an induction time of $\tau{\sim}120$, flow oscillation within the gap and downstream of the lower semicylinder depict a nice harmonic behavior. Here, the amplitude of the oscillations reaches a peak at a location of $(X, Y) = (5.5, 0)$ and decreases toward the downstream direction.

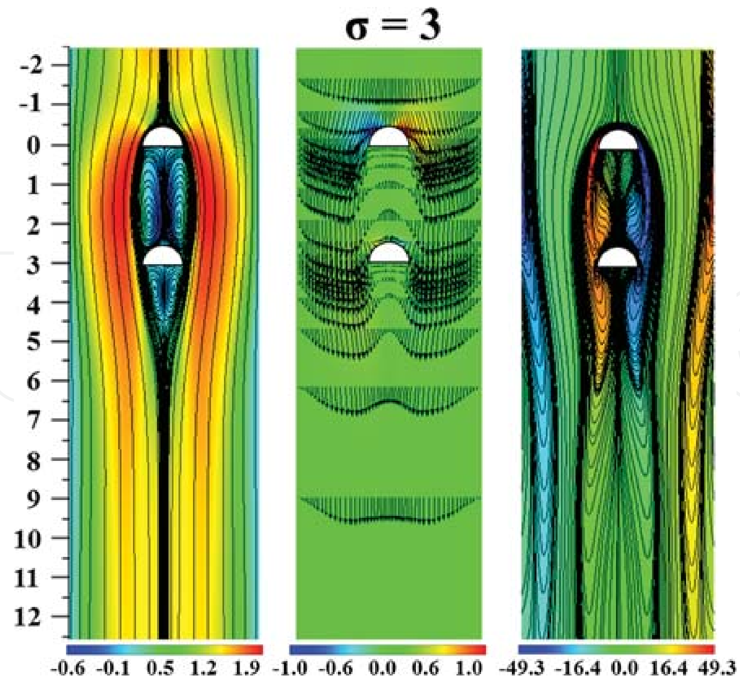

Figure 5. Nondimensional mean flow values for the unheated semicylinders at $Re_D = 200$, $BR = 0.2$, $\sigma = 3$, and $Ri = 0$. From left to right: U and V velocity and Ω vorticity fields, respectively.

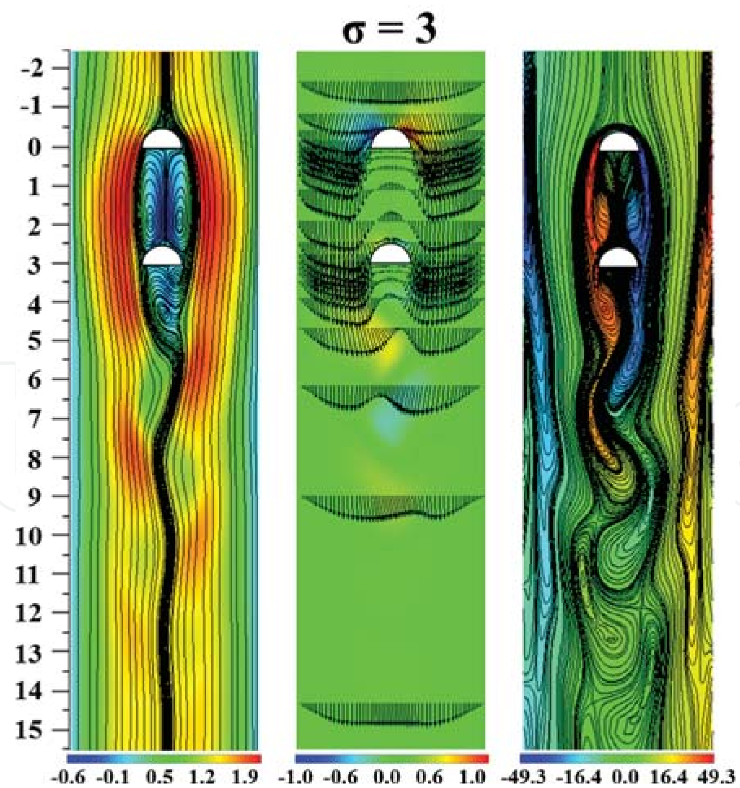

Figure 6. Nondimensional near-wake patterns of instantaneous velocity and vorticity contours for the unheated semicylinders at $Re_D = 200$, $BR = 0.2$, $\sigma = 3$, and $Ri = 0$. From left to right: U and V velocity and Ω vorticity fields, respectively.

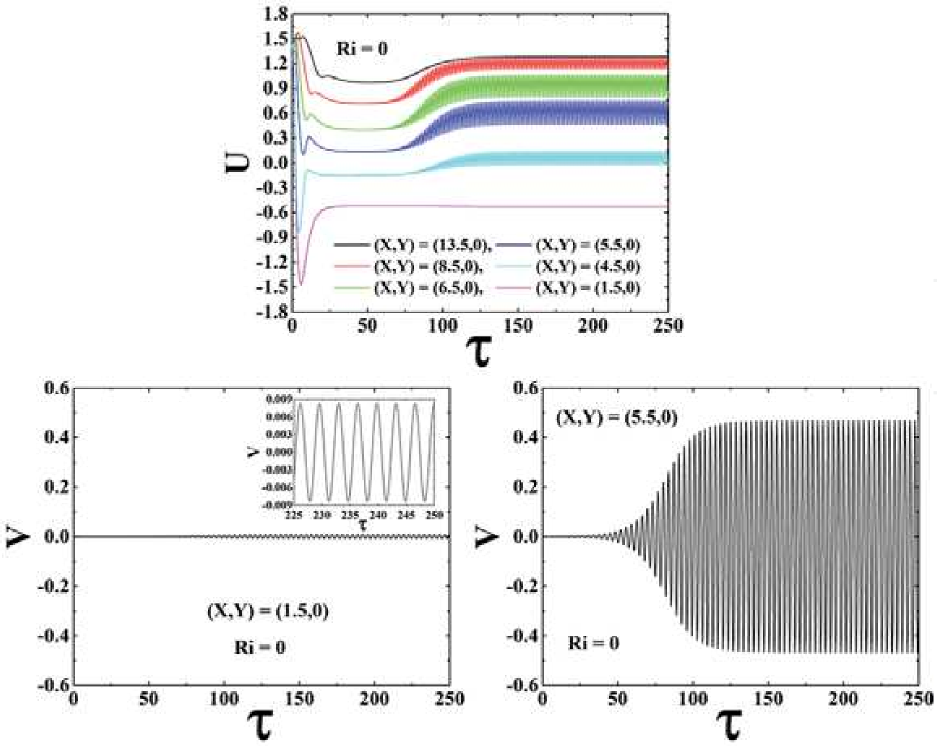

Figure 7. Time variations of the nondimensional longitudinal and transverse velocity components as a function of the nondimensional time at $Re_D = 200$, $BR = 0.2$, $\sigma = 3$, and $Ri = 0$. The extracted data is obtained at the symmetry plane and several X positions.

3.3. Response characteristics for opposing flow $(Ri = 1)$

In this section, the response characteristics for opposing flow are presented. **Figure 8** shows the nondimensional mean flow values at $Ri = 1$ $(Gr = 4 \times 10^4)$. Clearly, because of the presence of flow reversal, the width of the symmetric recirculation zone present within the gap and at the rear of the downstream semicylinder increases. As a result, the blockage effect is enhanced and the longitudinal velocity component reaches peak values close to the semicylinders. Note how due to secondary flow, both recirculation zones behind each semicylinder have approximately the same size. Also, because of the presence of relatively strong upward flow within the gap, a bridge that reconnects the thermal layers of both semicylinders increases buoyancy strength and vorticity strength reduces.

Figure 9 shows a typical instantaneous flow and thermal pattern at $Ri = 1$ $(Gr = 4 \times 10^4)$, illustrating how the shedding process changes in the presence of flow reversal. Here, the recirculation zone within the gap impinges the forebody of the downstream semicylinder and pairs periodically with the vortices shed by the downstream semicylinder. Note how because of the presence of relatively high upward flow, the downstream semicylinder sheds typical Kármán vortices of relatively large size. The third strip illustrates how vorticity contours become more complex toward the downstream direction. Here, A highlights how wall vorticity merges with downstream vortices with the same sign. The fourth strip shows how the total surface of the downstream semicylinder is completely surrounded by upward flow that produces a thermal plume at the upper stagnation point of the lower hemisphere. As such, heat transfer decreases because of the presence of relatively high temperature fluid within the gap.

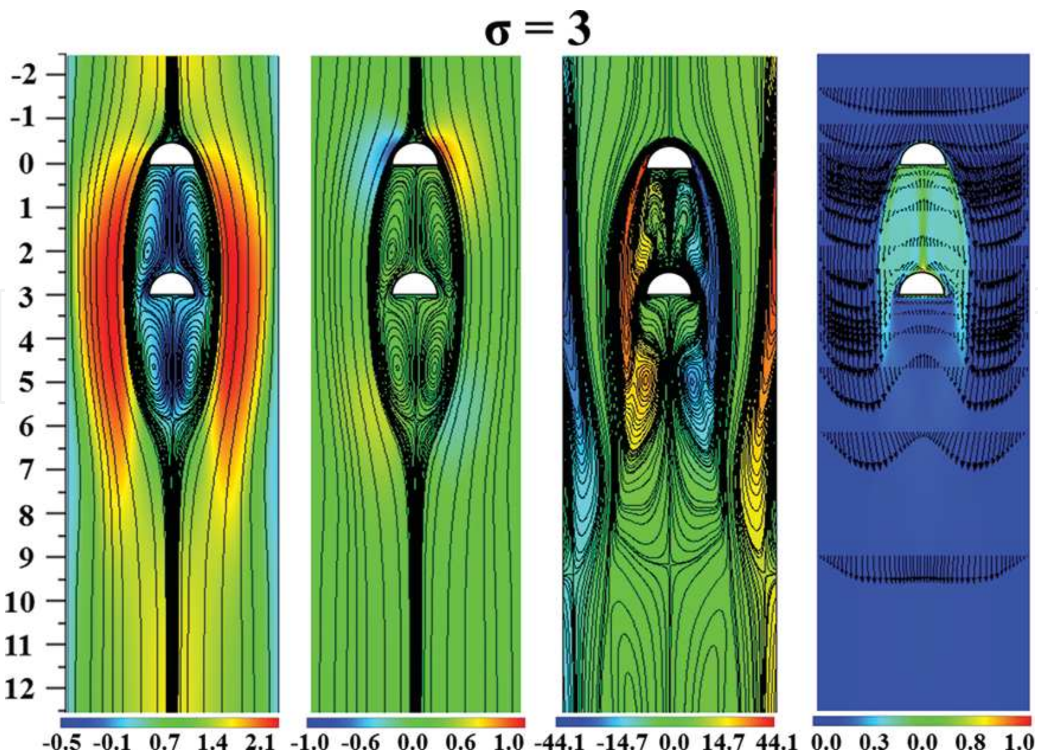

Figure 8. Nondimensional mean flow vales at $Re_D = 200$, $BR = 0.2$, $\sigma = 3$, and $Ri = 1$ ($Gr = 4 \times 10^4$). From left to right: U and Vvelocity, Ω vorticity and θ temperature fields, respectively.

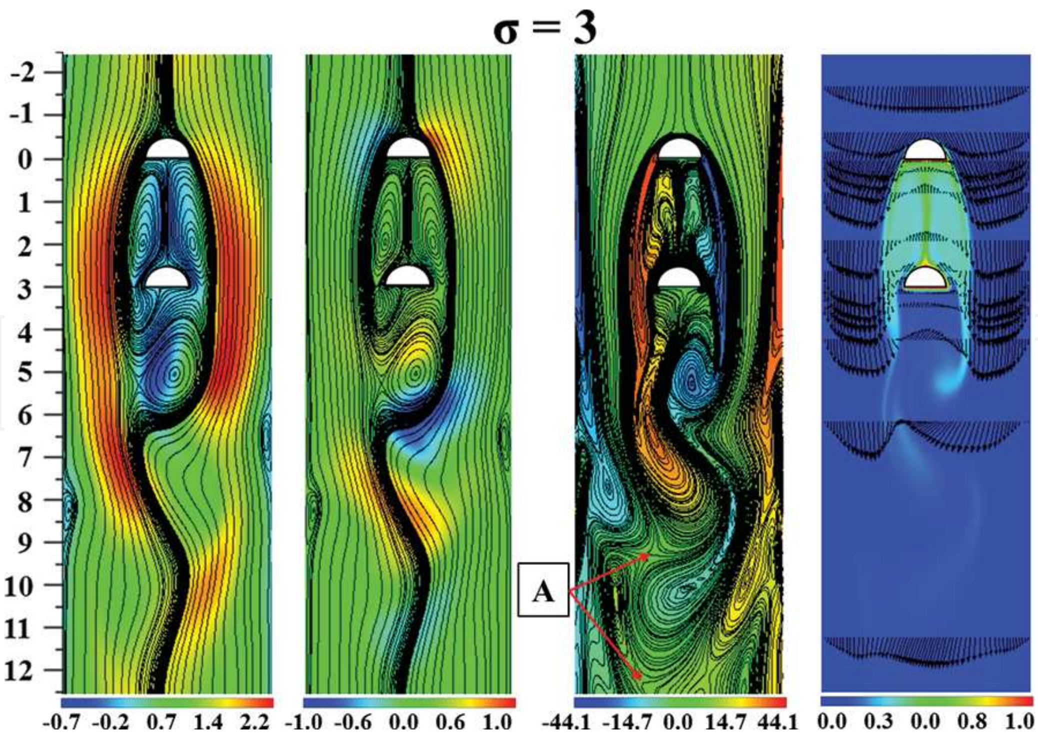

Figure 9. Nondimensional near-wake patterns of instantaneous velocity, vorticity and temperature contours at $Re_D = 200$, $BR = 0.2$, $\sigma = 3$, and $Ri = 1$ ($Gr = 4 \times 10^4$). From left to right: U and Vvelocity, Ω vorticity and θ temperature fields, respectively.

Figure 10 shows the time variations of the nondimensional longitudinal and transverse velocity components at the symmetry plane and selected longitudinal positions inside the channel. Clearly, time-periodic flow oscillation sets in after an induction time. The inset of the lower left image shows how the recirculation zone within the gap depicts periodic flow oscillation of relatively small amplitude.

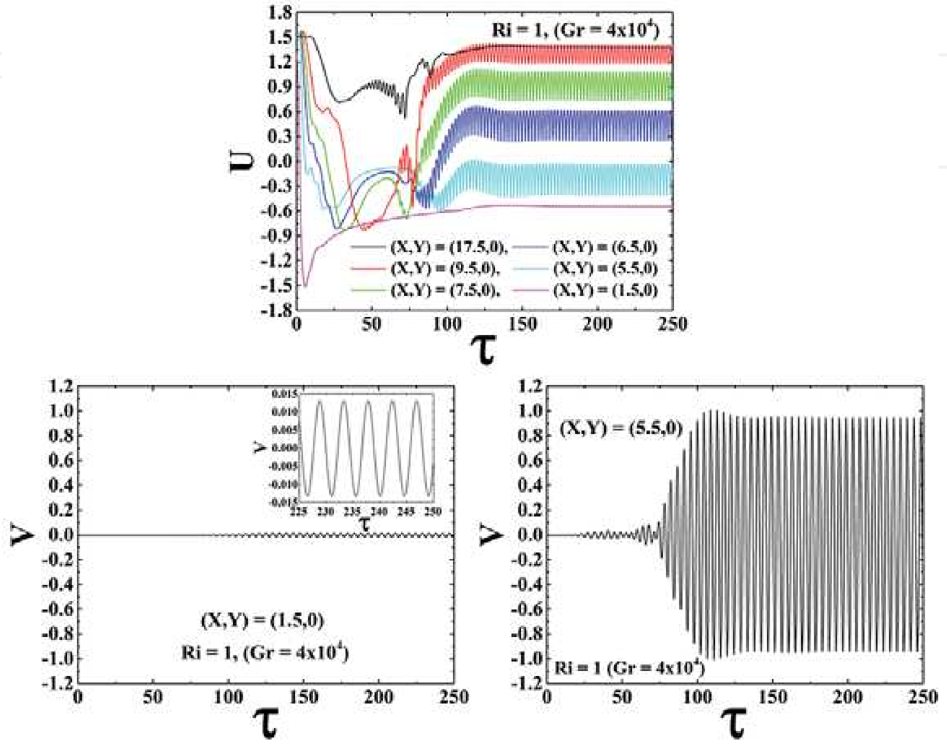

Figure 10. Time variations of the nondimensional longitudinal and transverse velocity components as a function of the nondimensional time at $Re_D = 200$, $BR = 0.2$, $\sigma = 3$, and $Ri = 1$ ($Gr = 4 \times 10^4$). The extracted data is obtained at the symmetry plane and several X positions.

3.4. Strouhal number and phase space plots

The left images in **Figure 11** show (from top to bottom) the normalized spectrum of the transverse velocity component as a function of the nondimensional frequency (Strouhal number), $St = fD/u_0$ for $Ri = -1$, 0 and 1, respectively.

These images show how for $Ri = -1$, 0 and 1 and for selected locations within the gap and downstream of the lower semicylinder, there is a sharp peak at $St = 0.32111$, 0.29448, and 0.22295, respectively, indicating that the wake vortex shedding of both semicylinders is time-periodic and is dominated by a single fundamental frequency. These images exemplify how for the three values of the buoyancy parameter studied, the recirculation zone of the upstream semicylinder locks on to the shedding frequency of the downstream one. In addition, these images show how the Strouhal number decreases for increasing values of the buoyancy parameter. The right images in **Figure 11** show the corresponding phase-space relation between the longitudinal and transverse velocity signals after the vortex shedding reaches an established periodicity. The inset of these figures describe the fluctuations at a location of $(X, Y) = (1.5, 0)$. For all cases, the single orbit with a double loop illustrates how the periodic alternate shedding of vortices takes place at the space within the gap and downstream of the lower semicylinder.

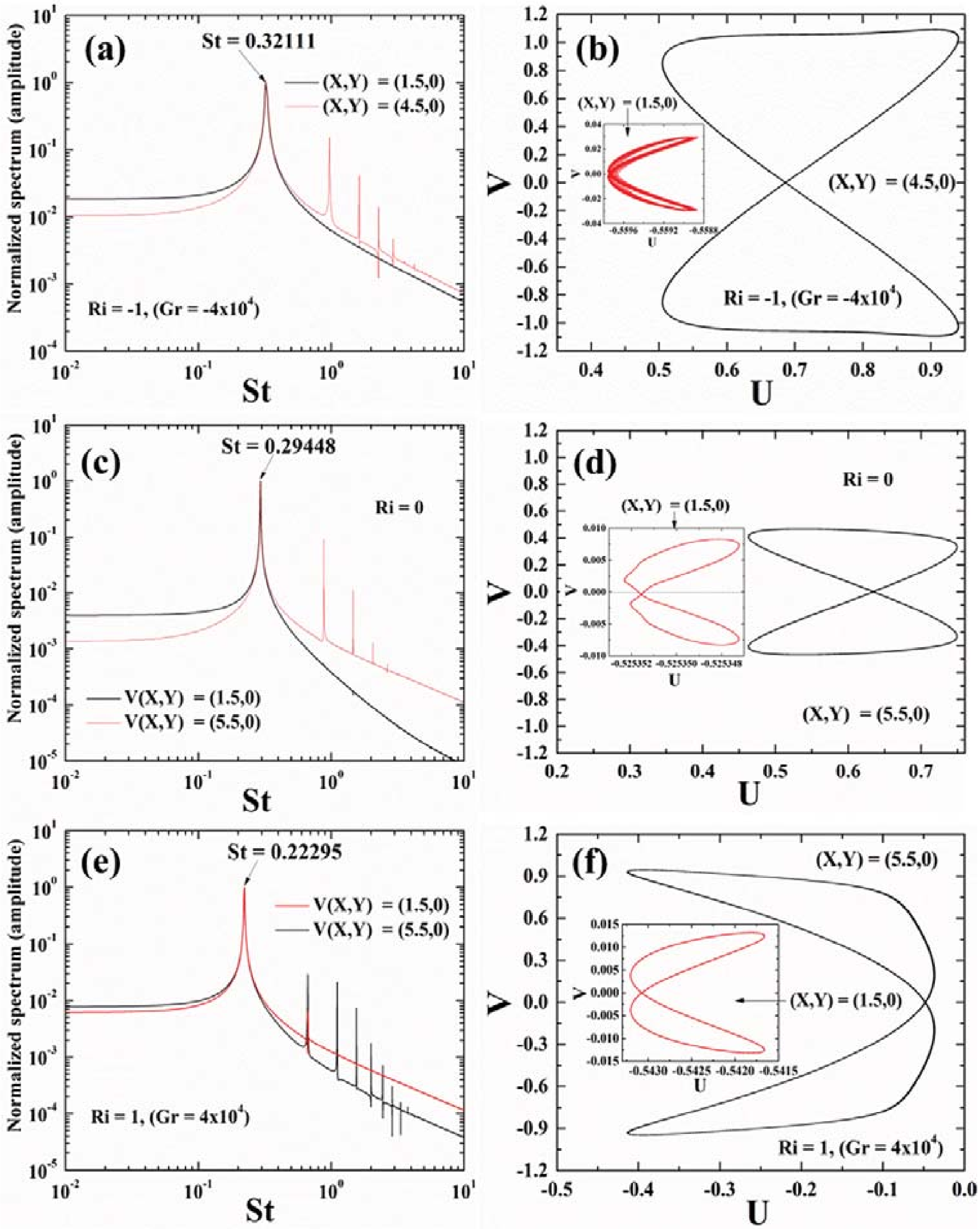

Figure 11. $Re_D = 200$, $BR = 0.2$, $\sigma = 3$, and $Ri = -1$, 0 and 1. Left images: Normalized spectrum of the longitudinal and transverse velocities. Right images: Phase-space plot of the longitudinal velocity signal as a function of the transverse velocity signal.

4. Heat transfer

In this section, the heat transfer characteristics of the semicylinder array are presented for buoyancy assisting and opposing flow.

4.1. Local Nusselt numbers

Figures 12a and **b** show representative distributions of the local Nusselt number defined in Eq. (8) over the curve length ***A-B-C-D*** (body contour of each semicylinder) for $Ri = -1$ and $Ri = 1$, respectively. In these figures, the broken and continuous lines correspond to the upstream and downstream semicylinder, respectively. For assisting/opposing buoyancy, when the warm/cold downward flow impinges the front stagnation point of the upstream semicylinder, the temperature gradient is maximum and the local Nusselt number reaches its peak value at point ***C***. Beyond point ***C***, as the warm/cold downward-flowing fluid travels through the front half of the semicylinder along the surface ***B-C-D***, it yields/picks up thermal energy and the local Nusselt number gradually decreases toward points ***B*** and ***D***. The cold/warm upward flow present between both semicylinders impinges the rear of the upstream one, a local maximum is reached at point ***A*** and a progressive increase in the local Nusselt number is observed over the curve length ***B-D***. Depending on whether buoyancy assists/opposes the flow and because of the presence of the recirculation zone within the gap that yields/picks up thermal energy from the wake of the upstream semicylinder, a local minimum of the local Nusselt number is reached at the front stagnation point of the downstream semicylinder. Thus, the local Nusselt number beyond point ***C*** gradually increases toward points ***B*** and ***D***. As the flow detaches from the tip of the downstream semicylinder (points ***B*** and ***D***), the local Nusselt number reaches a local/global maximum for assisting/opposing buoyancy, respectively.

4.2. Overall Nusselt number

Figure 13 shows the time variation of the surface-averaged Nusselt number of both semicylinders with Richardson number. In these figures, the broken and continuous lines correspond to the upstream and downstream semicylinder, respectively. **Figure 13** shows how the presence of the upstream semicylinder has a significant effect on the heat transfer characteristics of the downstream semicylinder and lower heat transfer rates are achieved by the latter. For clarity, in the inset of **Figure 13**, the value of the mean Nusselt number of both semicylinders is plotted in a limited range of the nondimensional time, from $\tau = 180$ to 200. It is worth to mention that the discernible periodic oscillations of the mean Nusselt number of the lower semicylinder are closely related to flow oscillation due to vortex shedding for both cases.

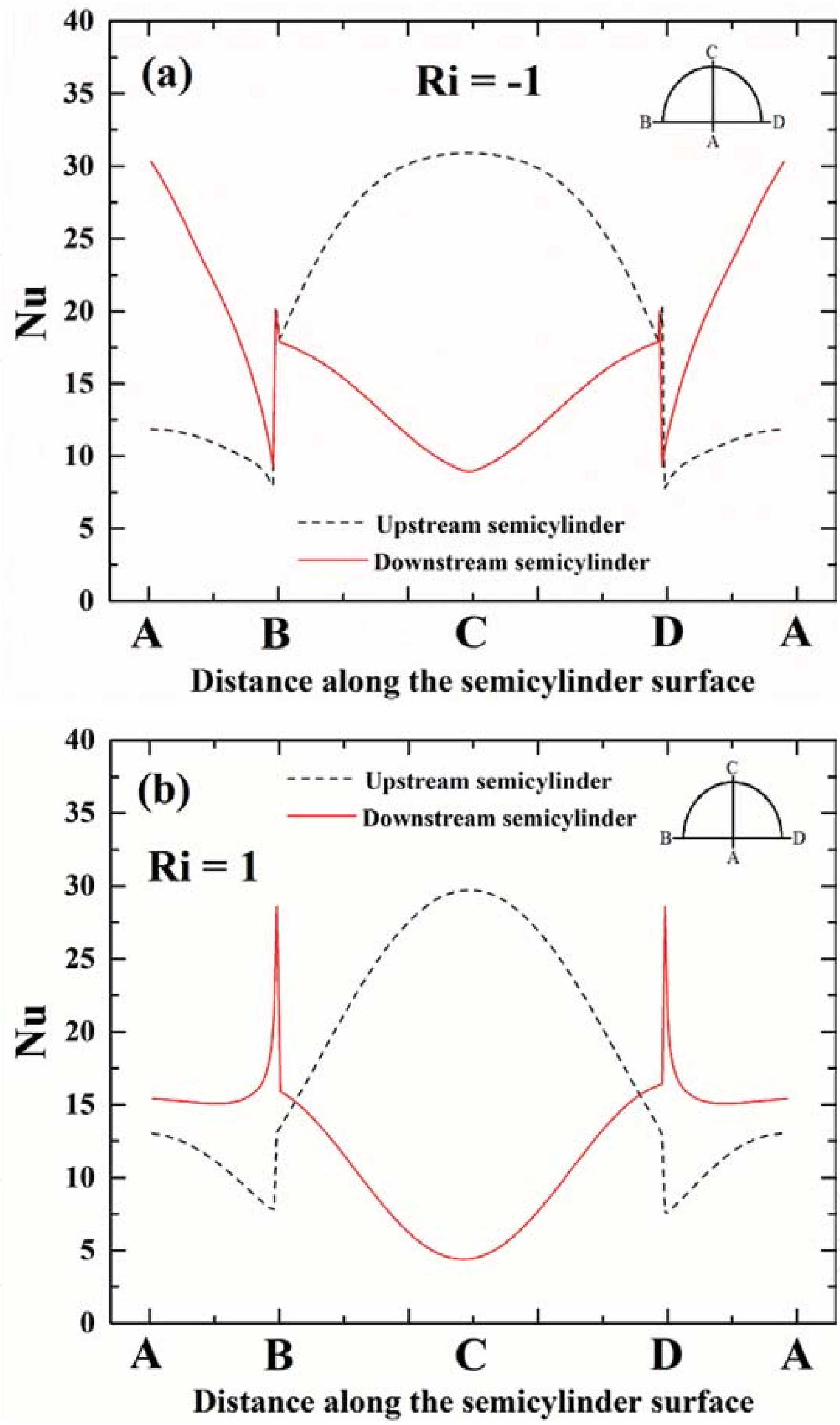

Figure 12. Distribution of the local Nusselt number on the surface of each semicylinder versus distance along each semicylinder surface for $Re_D = 200$, $BR = 0.2$, $\sigma = 3$, and $Ri = -1$ and 1, respectively.

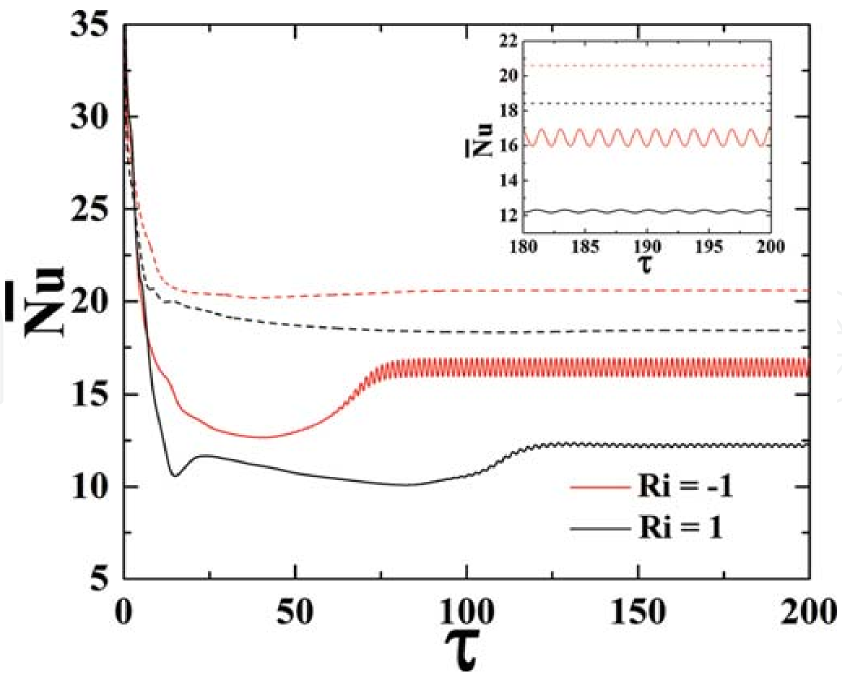

Figure 13. Time-evolution of the overall Nusselt numbers at $Re_D = 200$, $BR = 0.2$, $\sigma = 3$, and $Ri = -1$ and $Ri = 1$ for the upstream (broken lines) and downstream (continuous lines) semicylinders, respectively.

5. Conclusions

In this work, numerical simulations have been carried out to study the unsteady flow and heat transfer characteristics around two identical isothermal semicylinders arranged in tandem and confined in a channel. The blockage ratio, Prandtl number and pitch-to-diameter are fixed at $BR = 0.2$, $\mathrm{Pr} = 7$ and $\sigma = 3$, respectively. Numerical simulations are performed using the control-volume method on a nonuniform orthogonal Cartesian grid. The immersed-boundary method is employed to identify the semicylinders confined inside the channel. The influence of buoyancy has been assessed on the resulting mean and instantaneous flow, vortex shedding properties, nondimensional oscillation frequencies (Strouhal numbers), phase-space portraits of flow oscillation, thermal fields and local and overall nondimensional heat transfer rates (Nusselt numbers) from each semicylinder. Results show that in this parameter space, the flow patterns reach a time-periodic oscillatory state, the recirculation zone of the upper semicylinder completely fills the space within the gap and vortex shedding from the lower semicylinder occurs. For values of the Richardson number of for $Ri = -1$ and $Ri = 1$, steady-state and time periodic oscillations of the mean Nusselt number are observed for the upstream and downstream semicylinder, respectively.

Acknowledgements

This research was supported by the Consejo Nacional de Ciencia y Tecnología (CONACYT), Grant No. 167474.

http://dx.doi.org/10.5772/66692

Nomenclature

BR	blockage ratio, D/H
D	semicylinder diameter (characteristic length)
f	vortex shedding frequency (Hz)
g	gravity acceleration
Gr	Grashof number based on semicylinder diameter, $Gr = g\beta(T_w - T_0)D^3/\nu^2$
h	local heat transfer coefficient
H	width of computational domain
k	thermal conductivity of fluid
L	pitch (centre-to-centre distance between two semicylinders)
L_{tot}	length of computational domain
n	normal direction
Nu	local Nusselt number (see Eq. (8))
$\overline{Nu}$	Average Nusselt number (see Eq. (9))
Pe	Peclet number, $Pe = u_0 D/\alpha$
Pr	Prandtl number, $Pr = \nu/\alpha$
Re	Reynolds number based on u_0, $Re = u_0 D/\nu$
Re_D	Reynolds number based on u_D, $Re = u_D D/\nu$
Ri	Richardson number based on semicylinder diameter, $Ri = Gr/Re^2$
S	surface area of immersed semicylinders
S_1	length from the origin to the channel outlet
St	Strouhal number based on semicylinder diameter, $St = fD/u_0$
t	time
T	temperature
T_0	fluid temperature at the channel inlet
T_w	temperature at the surface of the semicylinders
u, v	longitudinal and transverse velocity components, respectively
u_0	mean fluid velocity at the channel inlet
u_D	average longitudinal velocity over the semicylinders (see Eq. (10))
U	nondimensional longitudinal velocity component, $U = u/u_0$
V	nondimensional transverse velocity component, $V = v/u_0$
x, y	Cartesian rectangular coordinates
X	nondimensional longitudinal coordinate, $X = x/D$
Y	nondimensional transverse coordinate, $Y = y/D$

Greek symbols

α	thermal diffusivity of fluid
β	thermal volumetric expansion coefficient
μ	dynamic viscosity
ν	kinematic viscosity
ψ	nondimensional stream function
Ω	nondimensional vorticity
σ	nondimensional pitch-to-diameter ratio, $\sigma = L/D$

θ nondimensional temperature, $\theta = (T - T_0)/(T_w - T_0)$
τ nondimensional time

Subscripts

0 ambient or reference
1, 2 refers to the upstream and downstream semicylinder, respectively
w at the surface of the semicylinders

Author details

Erick Salcedo[1], César Treviño[2], Juan C. Cajas[3] and Lorenzo Martínez-Suástegui[4]*

*Address all correspondence to: lamartinezs@ipn.mx

1 Departamento de Termofluidos, Facultad de Ingeniería, UNAM México, Ciudad de México, Mexico

2 UMDI, Facultad de Ciencias, Universidad Nacional Autónoma de México, Sisal, Yucatán, Mexico

3 Barcelona Supercomputing Center (BSC), Barcelona, Spain

4 ESIME Azcapotzalco, Instituto Politécnico Nacional, Ciudad de México, Mexico

References

[1] Hu H, Koochesfahani MM. Thermal effects on the wake of a heated circular cylinder operating in mixed convection regime. Journal of Fluid Mechancis. 2011;**685**:235–270. DOI: http://dx.doi.org/10.1017/jfm.2011.313.

[2] Khan WA, Culham JR, Yovanovich MM. Fluid flow and heat transfer from a cylinder between parallel plates. Journal of Thermophysics and Heat Transfer. 2004;**18**(3):395–403. DOI: http://dx.doi.org/10.2514/1.6186.

[3] Perng SW, Wu HW. Buoyancy-aided/opposed convection heat transfer for unsteady turbulent flow across a square cylinder in a vertical channel. International Journal of Heat and Mass Transfer. 2007;**50**(19–20):3701–3717. DOI: http://dx.doi.org/10.1016/j.ijheatmasstransfer.2007.02.026.

[4] Sarkar S, Dalal A, Biswas G. Unsteady wake dynamics and heat transfer in forced and mixed convection past a circular cylinder in cross flow for high Prandtl numbers. International Journal of Heat and Mass Transfer. 2011;**54**(15–16):3536–3551. DOI: http://dx.doi.org/10.1016/j.ijheatmasstransfer.2011.03.032.

[5] Sharma N, Dhiman AK, Kumar S. Mixed convection flow and heat transfer across a square cylinder under the influence of aiding buoyancy at low Reynolds numbers. International Journal of Heat and Mass Transfer. 2012;**55**:2601–2614. DOI: http://dx.doi.org/10.1016/j.ijheatmasstransfer.2011.12.034.

[6] Lima E Silva ALF, Silveira-Neto A, Damasceno JJR. Numerical simulation of two-dimensional flows over a circular cylinder using the immersed boundary method. Journal of Computational Physics. 2003;**189**:351–370. DOI: http://dx.doi.org/10.1016/S0021-9991(03)00214-6.

[7] Kondjoyan A, Daudin JD. Effects of free stream turbulence intensity on heat and mass transfer at the surface of a circular and elliptic cylinder, axis ratio 4. International Journal of Heat and Mass Transfer. 1995;**38**:1735–1749. DOI: 10.1016/0017-9310(94)00338-V.

[8] Liao CC, Lin CA. Influences of a confined elliptic cylinder at different aspect ratios and inclinations on the laminar natural and mixed convection flows. International Journal of Heat and Mass Transfer. 2012;**55**:6638–6650. DOI: http://dx.doi.org/10.1016/j.ijheatmasstransfer.2012.06.073.

[9] Paul I, Prakash KA, Vegadesan S. Forced convective heat transfer from unconfined isothermal and isoflux elliptic cylinders. Numerical Heat Transfer, Part A: Applications. 2013;**64**:648–675. DOI: http://dx.doi.org/10.1080/10407782.2013.790261.

[10] Richter A, Nikrityuk PA. New correlations for heat and fluid flow past ellipsoidal and cubic particles at different angles of attack. Powder Technology. 2013;**249**:463–474. DOI: http://dx.doi.org/10.1016/j.powtec.2013.08.044.

[11] Bruno L, Salvetti MV, Ricciardelli F. Benchmark on the aerodynamics of a rectangular 5:1 cylinder: an overview after the first four years of activity. Journal of Wind Engineering and Industrial Aerodynamics. 2014;**126**:87–106. DOI: http://dx.doi.org/10.1016/j.jweia.2014.01.005.

[12] Igarashi T. Fluid flow and heat transfer around rectangular cylinders (the case of a width/height ratio of a section of 0.33–1.5). International Journal of Heat and Mass Transfer. 1987;**30**:893–901. DOI: doi:10.1016/0017-9310(87)90008-1.

[13] Mannini C, Soda A, Schewe G. Unsteady RANS modelling of flow past a rectangular cylinder: investigation of Reynolds number effects. Computers and Fluids. 2010;**39**(9):1609–1624. DOI: http://dx.doi.org/10.1016/j.compfluid.2010.05.014.

[14] Okajima A, Yi D, Sakuda A, Nakano T. Numerical study of blockage effects on aerodynamic characteristics of an oscillating rectangular cylinder. Journal of Wind Engineering and Industrial Aerodynamics. 1997;**67–68**:91–102. DOI: 10.1016/S0167-6105(97)00065-2.

[15] Patruno L, Ricci M, de Miranda S, Ubertini F. Numerical simulation of a 5:1 rectangular cylinder at non-null angles of attack. Journal of Wind Engineering and Industrial Aerodynamics. 2016;**151**:146–157. DOI: http://dx.doi.org/10.1016/j.jweia.2016.01.008.

[16] Dhiman AK, Chhabra RP, Sharma A., Eswaran V. Effects of Reynolds and Prandtl numbers on heat transfer across a square cylinder in the steady flow regime. Numerical Heat Transfer, Part A. 2006;**49**:717–731. DOI: doi/abs/10.1080/10407780500283325.

[17] Igarashi T. Heat transfer from a square prism to an air stream. International Journal of Heat and Mass Transfer. 1985;**28**(1):175–181. DOI: 10.1016/0017-9310(85)90019-5.

[18] Sohankar A, Norberg C, Davidson L. Low Reynolds number flow around a square cylinder at incidence: study of blockage, onset of vortex shedding and outlet boundary condition. International Journal for Numerical Methods in Fluids. 1998;**26**:39–56. DOI: 10.1002/(SICI)1097-0363(19980115)26:1<39::AID-FLD623>3.0.CO;2-P.

[19] Tong JCK, Sparrow EM, Minkowycz WJ, Abraham JP. A new archive of heat transfer coefficients from square and chamfered cylinders at angles of attach in crossflow. International Journal of Thermal Sciences. 2016;**105**:218–223. DOI: http://dx.doi.org/10.1016/j.ijthermalsci.2016.03.008.

[20] Yoo SY, Goldstein RJ, Chung MK. Effects of angle of attack on mass transfer from a square cylinder and its base plate. International Journal of Heat and Mass Transfer. 1993;**36**:371–381. DOI: 10.1016/0017-9310(93)80013-K.

[21] Chandra A, Chhabra RP. Flow over and forced convection heat transfer in Newtonian fluids from a semi-circular cylinder. International Journal of Heat and Mass Transfer. 2011;**54**:225–241. DOI: http://dx.doi.org/10.1016/j.ijheatmasstransfer.2010.09.048.

[22] Chandra A, Chhabra RP. Laminar free convection from a horizontal semi-circular cylinder to power-law fluids. International Journal of Heat and Mass Transfer. 2012;**55**:2934–2944. DOI: http://dx.doi.org/10.1016/j.ijheatmasstransfer.2012.02.034.

[23] Sasmal C, Shyam R, Chhabra RP. Laminar flow of power-law fluids past a hemisphere: momentum and forced convection heat transfer characteristics. International Journal of Heat and Mass Transfer. 2013;**63**:51–64. DOI: http://dx.doi.org/10.1016/j.ijheatmasstransfer.2013.03.059.

[24] Tiwari AK, Chhabra RP. Laminar natural convection in power-law liquids from a heated semi-circular cylinder with its flat side oriented downward. International Journal of Heat and Mass Transfer. 2013;**58**:553–567. DOI: http://dx.doi.org/10.1016/j.ijheatmasstransfer.2012.11.051.

[25] Gode A, Sahu AK, Chhabra RP. Two-dimensional steady flow over a semi-circular cylinder: drag coefficient and Nusselt number. International Journal of Advances in Engineering Sciences and Applied Mathematics. 2011;**3**(1–4):44–59. DOI: 10.1007/s12572-011-0039-6.

[26] Boisaubert N, Texier A. Effect of a splitter plate on the near-wake development of a semi-circular cylinder. Experimental Thermal and Fluid Science. 1998;**16**:100–111. DOI: http://dx.doi.org/10.1016/S0894-1777(97)10009-7.

[27] Nalluri SV, Patel SA, Chhabra RP. Mixed convection from a hemisphere in Bingham plastic fluids. International Journal of Heat and Mass Transfer. 2015;**84**:304–318. DOI: http://dx.doi.org/10.1016/j.ijheatmasstransfer.2014.12.059.

[28] Bhinder APS, Sarkar S, Dalal A. Flow over and forced convection heat transfer around a semi-circular cylinder at incidence. International Journal of Heat and Mass Transfer. 2012;**55**:5171–5184. DOI: http://dx.doi.org/10.1016/j.ijheatmasstransfer.2012.05.018.

[29] Chandra A, Chhabra RP. Mixed convection from a heated semi-circular cylinder to power-law fluids in the steady flow regime. International Journal of Heat and Mass Transfer. 2012;**55**:214–234. DOI: http://dx.doi.org/10.1016/j.ijheatmasstransfer.2011.09.004.

[30] Kumar A, Dhiman A, Baranyi L. CFD analysis of power-law fluid flow and heat transfer around a confined semi-circular cylinder. International Journal of Heat and Mass Transfer. 2015;**82**:159–169. DOI: http://dx.doi.org/10.1016/j.ijheatmasstransfer.2014.11.046.

[31] Thom A. The flow past circular cylinders at low speeds. Proceedings of the Royal Society A. 1933;**41**:651–669. DOI: 10.1098/rspa.1933.0146.

[32] Mittal R, Iaccarino G. Immersed boundary methods. Annual Review of Fluid Mechanics. 2005;**37**:239–261. DOI: 10.1146/annurev.fluid.37.061903.175743.

[33] Patankar S. Numerical Heat Transfer and Fluid Flow. 1st ed. United States of America: Hemisphere Publishing Corporation; 1980. 214 p. DOI: ISBN 9780891165224.

[34] Mittal R, Dong H, Bozhurttas M, Najjar F, Vargas A, von Leobbecke A. A versatile sharp interface immersed boundary method for incompressible flows with complex boundaries. Journal of Computational Physics. 2008;**227**(10):4825–4852. DOI: 10.1016/j.jcp.2008.01.028.

[35] Chen JH, Pritchard WG, Tavener SJ. Bifurcation of flow past a cylinder between parallel plates. Journal of Fluid Mechanics. 1995;**284**:23–41. DOI: http://dx.doi.org/10.1017/S0022112095000255.

[36] Martínez-Suástegui L, Treviño C. Transient laminar opposing mixed convection in a differentially and asymmetrically heated vertical channel of finite length. International Journal of Heat and Mass Transfer. 2008;**51**(25–26):5991–6005. DOI: 10.1016/j.ijheatmasstransfer.2008.04.055.

[37] Salcedo E, Cajas JC, Treviño C, Martínez-Suástegui L. Unsteady mixed convection heat transfer from two confined isothermal circular cylinders in tandem: buoyancy and tube spacing effects. International Journal of Heat and Fluid Flow. 2016;**60**:12–30. DOI: http://dx.doi.org/10.1016/j.ijheatfluidflow.2016.04.001.